Title

Standardization of mineral density maps of physiologic and pathologic biominerals in humans using cone-beam CT and micro-CT scanners

Journal

Dental Materials, 38(6)

ISSN

0109-5641

Authors

Srirangapatanam, Sudarshan
Kang, Misun
Ellenikiotis, Yianni
et al.

Publication Date

2022-06-01

DOI

10.1016/j.dental.2022.03.010

Peer reviewed

DENTAL MATERIALS 38 (2022) 989–1003

Available online at www.sciencedirect.com

ScienceDirect

journal homepage: www.elsevier.com/locate/dental

Standardization of mineral density maps of physiologic and pathologic biominerals in humans using cone-beam CT and micro-CT scanners

Sudarshan Srirangapatanam[a,b], *Misun Kang*[c], *Yianni Ellenikiotis*[d], *Andrew Jheon*[d], *Sunil Kapila*[d], *Hubert S. Swana*[b], *Marshall L. Stoller*[a], *Youngho Seo*[e,f], *Sunita P.Ho*[a,c,*]

[a] *Department of Urology, School of Medicine, University of California, San Francisco, CA, USA*
[b] *College of Medicine, University of Central Florida, FL, USA*
[c] *Department of Preventive and Restorative Dentistry, School of Dentistry, University of California, San Francisco, CA, USA*
[d] *Department of Orofacial Sciences, School of Dentistry, University of California, San Francisco, CA, USA*
[e] *Department of Radiology and Biomedical Imaging, School of Medicine, University of California, San Francisco, CA, USA*
[f] *Department of Nuclear Engineering, University of California Berkeley, Berkeley, CA, USA*

ARTICLE INFO

Article history:
Received 15 December 2021
Received in revised form 4 March 2022
Accepted 19 March 2022

Keywords:
Craniofacial and dental tissues
Skeletal bone
X-ray imaging
Computed tomography
Mineral density

ABSTRACT

Objectives: The lack of standardized X-ray imaging remains a challenge for comparative studies on spatial scans acquired from different clinic-specific X-ray scanners. The central objectives of this study are: **1)** to delineate mineral density (MD) values, and **2)** generate spatial MD maps of various physiologic and pathologic biominerals, and **3)** propose a standardization protocol within the safe-operating zone of a CT scanner that underpins normalization of absorbed dose to shape and density of tissues.

Methods: A systematic approach to propose a standardization protocol for CT imaging *in vivo* included: 1) estimation of pathologic MD ranges by performing a comparative meta-analysis on 2009–2019 data from the PubMed database; 2) calibration of cone-beam CT (CBCT) and micro-CT scanners with phantoms of known mineral densities (0, 250, 500, 750 and 3000 mg/cc) and shapes (cylinders and polyhedrons); 3) scanning craniofacial bones (N = 5) and dental tissues (N = 5), and ectopic minerals from humans (N = 3 each, pulp, salivary gland, kidney and prostrate stones, and penile and vascular plaques); 4) underscoring the effect of shape-factor (surface area-to-volume ratio) on MD of biominerals.

Results: Higher MDs of physiologic and pathologic cortical bones (504–1009 mg/cc) compared to trabecular bone (82–212 mg/cc) were observed. An increase in shape-factor in-

* Correspondence to: 813 Health Sciences West (HSW), 513 Parnassus Avenue, San Francisco, CA 94143, USA.
E-mail address: Sunita.Ho@ucsf.edu (S.P. Ho).

https://doi.org/10.1016/j.dental.2022.03.010

creased the CBCT error in MD measurement and revealed that the scanner resolution is dependent on the absorbed dose and shape-factor of detectable features.

Significance: CT scanners should be calibrated with phantoms containing segments of known shape-factors and mineral densities to identify safe-operating zones. The calibrated approach will narrow the gap between length-scale dependent measurements, and will permit spatiotemporal quantitative and reliable detection of pathologies.

1. Introduction

Radiodense pathologic biominerals can be visualized throughout the human body using X-ray computed tomography (CT) scanners. Biominerals typically form locally through complex processes that involve dynamic interactions between the organic and inorganic constituents [1]. The early stages of these mineralizing nodules cannot be seen with routine clinical CTs that are designed to image macrometer sized pathologies.

These unseen or at times overlooked lower density mineralized beginnings of pathologic biominerals are in fact spatially highly-ordered (as seen with micro CT), with their size, shape, and chemical composition determined by their unique environments. From a practical standpoint, patient treatments are based on the observed macro-scale pathology, which likely represents a late-stage of a disease that requires invasive interventions or is no longer treatable [2]. In the absence of standard imaging protocols, the undesirable knowledge gap between biological events and their progression into clinically detectable pathology will remain an insurmountable hurdle in rendering timely and optimal care.

Radiographic imaging in medicine and dentistry provides clinicians with a visual representation of anatomy with limited to no information on the pathophysiology of associated diseases [3–5]. Different X-ray technologies have contributed to a routine use of non-standardized imaging protocols on patients [6,7]. Partly for this reason, the reliable detection of initial disease states using non-invasive imaging with the goal of prevention or early treatment remains a challenge. This raises several questions that include: **1)** Can existing extensive data in the literature on mineral densities help delineate differences between physiologic and pathologic biominerals? **2)** Can early-stage microscopic changes that can evolve into pathologic biominerals be detected with current clinical X-ray technologies? **3)** Can current X-ray imaging technologies characterize pathology at varied length-scales; an early-stage micro-scale radiodense biomineral within a macro-scale human? To answer these questions, the objectives of this study are to: **1)** identify and contrast the published ranges and averages of physiologic with pathologic mineral densities of the same tissue types from the PubMed database; **2)** calibrate X-ray CT scanners to generate quantitative spatial maps of mineral densities in milligrams per cubic volume (mg/cc) of radiopaque tissues; **3)** identify the sources of error in mineral density (MD) measurement within and across CBCT and micro-CT scanners; **4)** propose a standardization protocol within the safe operating zone that would enable clinicians to generate reliable quantitative spatial MD maps for patients by estimating the scanner error. The overall goal for this study is to empower clinicians with a systematic workflow that can reliably delineate the health status of scanned mineralized tissues. Standardized protocols also will allow scans from different medical centers and scanners to be compared as clinicians follow their patients across multiple locations. In essence, a standardization protocol that delineates pathologies through quantitative scans irrespective of imaging centers can be envisioned [8–11]. More specifically, the newer quantitative methodologies will: **a)** consolidate the commonly observed absorbed dose in gray scale to Hounsfield units (HU), and from HU to MD (mg/cc) units of different X-ray scanning technologies across length scales; **b)** underpin the effects of shapes and sizes of objects through shape-factor as a ratio of surface area to volume of an object on MD regardless of the scanner technology; and **c)** underscore the length-scale specific shape-factor effect on measured mineral densities of biominerals. Finally, this calibrated systemic approach will provide reliable mineral densities of skeletal and craniofacial bones, dental tissues, and ectopic biominerals and enable an atlas of these physiologic and pathologic biominerals from humans.

2. Materials and Methods

2.1. *Meta-data collection and analyses*

Published mineral densities categorized as physiologic and pathologic biominerals, including renal diseases, osteoporosis, arthritis, diabetes mellitus, hypophosphatasia, and hypophosphatemia (see Supplemental Table 1 for a full list of pathologies) were extracted from 2009 to 2019 PubMed literature. Articles reporting any surgical or pharmacological interventions prior to the MD measurements were excluded. Three separate search queries were used to generate skeletal, craniofacial cortical and trabecular bones, and dental tissues (Fig. 1) categories. The search queries included the use of “mineral density” or “Hounsfield units” as reporting units of mineral densities. Original journal articles in English that investigated adult humans were included in the initial data collection. Original research articles matching the search queries were further sorted using filters that included sample size (number of patients and specimens), average MD, and MD standard deviation or error values.

A. Search queries for literature review

Specimen category	Search query
Cortical bone	**(cortical bone)** AND ((((("mineral density") OR ("Hounsfield Units")) AND (physiology OR pathology OR pathologic OR physiologic)) AND ("english"[Language])) AND ("journal article"[Publication Type]) AND (humans[Filter]) AND (alladult[Filter]) AND (2009:2019[pdat])
Trabecular bone	**(trabecular bone NOT "trabecular bone score")** AND ((((("mineral density") OR ("Hounsfield Units")) AND (physiology OR pathology OR pathologic OR physiologic)) AND ("english"[Language])) AND ("journal article"[Publication Type]) AND (humans[Filter]) AND (alladult[Filter]) AND (2009:2019[pdat])
Dental tissues	**(teeth OR dental OR tooth OR enamel OR dentin OR molar OR cementum)** AND ((((("mineral density") OR ("Hounsfield Units")) AND (physiology OR pathology OR pathologic OR physiologic)) AND ("english"[Language])) AND ("journal article"[Publication Type]) AND (humans[Filter]) AND (alladult[Filter]) AND (2009:2019[pdat])

B. Articles matching search queries

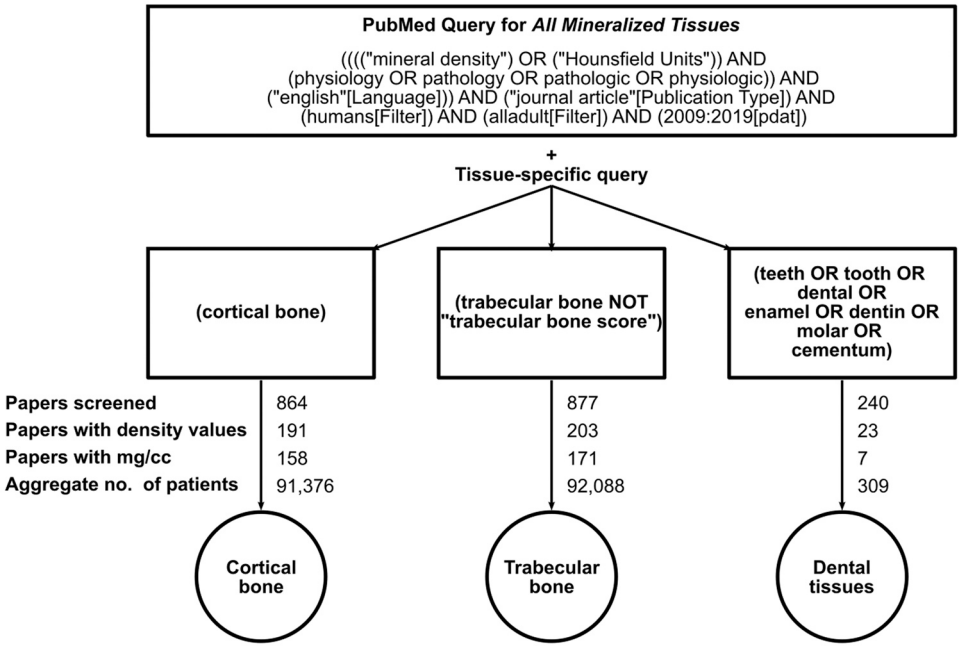

C. Scanning parameters used in literature*

	Cortical bone	Trabecular bone	Dental tissues
Current (mA)	209.1 ± 189.0	163.0 ± 65.5	60.0 ± 49.5
Voltage (kVp)	104.9 ± 23.5	98.2 ± 27.5	86.3 ± 38.8
Scanning speed (mm/s)	27.5 ± 3.5	23.3 ± 10.3	10 **
Voxel size (μm)	396.1. ± 187.2	357.4 ± 173.1	221.0 ± 209.1
Slice thickness (mm)	1.9 ± 0.7	1.9 ± 0.8	0.8 ± 0.6

All values show mean ± SD
* Data from representative set of articles; ** A single journal article reported scanning speed for dental tissues

Fig. 1 – *Flowchart to extract the published data on pathologic and physiologic biominerals.* A. Characterization of journal articles and data collection workflow. B. Illustration of the workflow and filters used in the PubMed database to establish MD dataset. C. Scanning parameters used in the literature from a representative set of journal articles were. A single journal article under dental tissues category reported scanning speed. All data show mean ± SD.

Anatomy-specific average mineral densities of skeletal (femur, vertebral bone, pelvic bone, radius and tibia), and craniofacial tissues and bones (alveolar bone, cementum, dentin, enamel, mandible and maxilla), and their respective two compartments (cortical and trabecular) were categorized accordingly. Meta-analysis with random-effects model using a restricted maximum-likelihood estimator was used to generate a pooled average MD (mg/cc). The pooled average was weighted using number of patients for each specimen type (e.g. cortical and trabecular bones) along with their respective 95% confidence intervals to establish reliable MD ranges. The inherent variabilities in measured mineral densities resulting from scanner resolution, age, and gender were mapped using the random-effects model. Meta-analysis was conducted using R statistical computing environment *version 4.0.2* with *meta for* package [12,13]. From the total number of articles extracted from the PubMed database matching the inclusion criteria, thirty articles were randomly selected as representative articles for each of the cortical and trabecular bone categories and twenty-three articles were selected for dental tissues category. These representative articles were further filtered for the type of scanner and scanning parameters to reveal if reported MD changes were anatomy-specific (cortical or trabecular within skeletal bone) (Fig. 1**C**).

2.2. *Calibration of CT scanners to generate quantitative MD spatial maps in mg/cc*

Two CBCT scanners (CBCT 1 and CBCT 2; Carestream CS 9300 and 8100, Carestream Dental LLC, Atlanta, GA, USA, respectively) and one micro-CT scanner were used to scan all specimens at different length scales (Fig. 3). Each scanner was calibrated to a set of cylindrical phantoms with known MD segments of 0, 100, 250, 500, and 750 mg/cc (CIRS Tissue Simulation & Phantom Technology, Norfolk, VA, USA). One segment of the phantom could be accommodated within the field of view (FOV) of the micro-CT (MicroXCT-200, Carl Zeiss X-ray Microscopy, Pleasanton, CA, USA) scanner compared to all segments within the FOV of CBCT 1 and 2 scanners. A current of 4 mA and voltage of 90 kVp and 84 kVp, were used when scanning using CBCT 1 and CBCT 2 respectively. The micro-CT was set to two different settings. The first setting was to a current and voltage of 0.198 mA and 40 kVp (micro XCT 1), and the second setting was to a current of 0.088 mA and a voltage of 90 kVp (micro XCT 2). Three different polyhedron sizes, small (16 mm^3), medium (77 mm^3), and large (467 mm^3), of hydroxyapatite of a standard MD (3000 mg/cc) were scanned separately using both CBCTs and micro-CT scanners at aforementioned settings. The exposure time per specimen for CBCT 1 was 12–23 s, with 429 projections, and a signal to noise ratio (SNR) of 3. The exposure time for CBCT 2 was 3–15 s, with 650 projections and an SNR of 4. The exposure time for micro-CT at 40 kVp was 33 s/projection, with 360 projections, and SNR of 5; and at 90 kVp was 4 s/projection, with 360 projections and an SNR of 5. Average gray values representative of absorbed dose, and Hounsfield units (HU) of each segment were plotted against the known MD value of that segment.

2.3. *Quantitative MD maps of biominerals*

Micro-CT at 4X magnification and 40 kVp was used to scan pathologic minerals from different anatomical locations of various patients. Tissues included, craniofacial bones (N = 5), and ectopic biominerals (N = 3) such as mineralized pulp, salivary, prostate, and kidney stones, and penile and vascular plaques. All specimens were collected intra-operatively at the University of California, San Francisco under institutional review board approval (IRB #14-14533 and protocol #H8933071801). To further delineate voltage-dependent structure resolution capabilities between CBCT and micro-CT scanners, specimens were scanned at 90 kVp using micro-CT to match the default peak voltage of the CBCT scanner. The digitally reconstructed images of the experimental specimens including ectopic biominerals were analyzed using AVIZO 2019.2 software (Fisher Scientific, Hillsboro, OR) to generate spatial maps of absorbed dose in gray values to mg/cc using the calibration curves for CBCT and micro-CT respectively.

2.4. *Quantification of error in MD measurements*

The surface area and volume of each specimen (calibration specimens, tissues of the teeth, and ectopic biominerals) in addition to MD were calculated from each digitally rendered volume. The shape-factor (SF) of each specimen was defined as the ratio of its surface area to volume (mm^{-1}). Shape-factor was considered to estimate error in MD measurements because the surface area and volume of a detectable feature are affected by spatial/voxel resolution of CT scanners. The variation in MD was quantified using standard error (SE) of average mineral densities observed in phantoms with known MD. Standard error was estimated as the ratio of standard deviation of measurements to the square root of the number of voxels. The safe operating spatial zones within which MD can be reliably measured using CBCT and micro-CT were mapped by identifying the contribution of shapes and sizes of ectopic biominerals to the standard error in MD measurements. Statistical analyses of SF was performed using a linear regression model that identified changes in measured errors in mineral densities per unit change in shape-factor.

3. Results

3.1. *Meta-data analysis of physiologic and pathologic bones and dental tissues extracted from the PubMed database (Figs. 1, 2)*

A total of 1981 articles between 2009 and 2019 reporting mineral densities of physiologic and pathologic bones and dental tissues were collected from the PubMed database (Fig. 1**A–C**). After applying the inclusion and exclusion criteria, 417 articles (Fig. 1**B**) illustrated voltage range from 12 kVp to 130 kVp with a voxel size range from 3.8 µm to 400 µm (Fig. 1**C**). The enlisted mineral densities of physiologic and pathologic mineralized tissues illustrated inherent heterogeneities regardless of the units in which they were published (either HU or mg/cc). Cortical bone, as expected was of

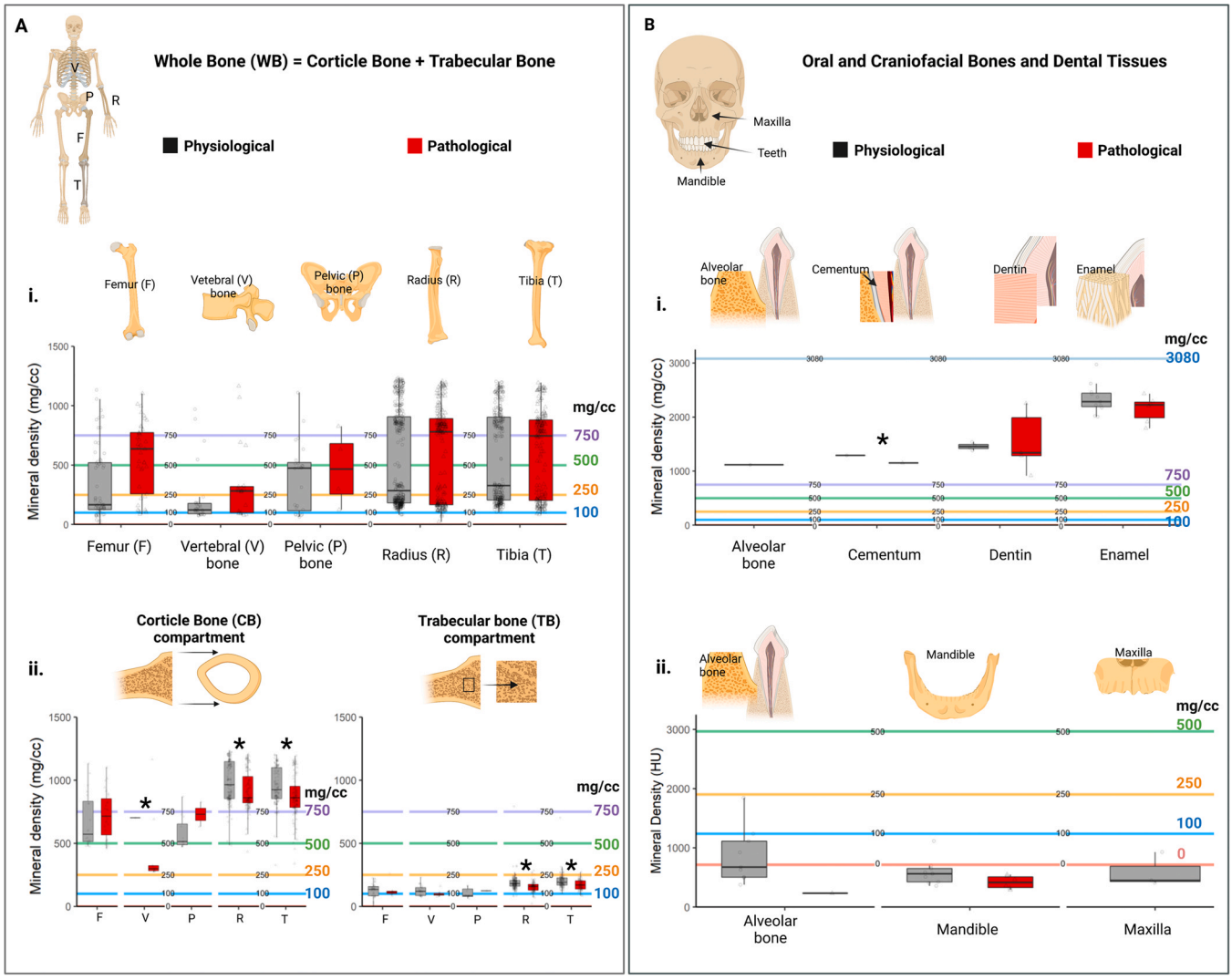

Fig. 2 – *Metadata of mineral densities of skeletal and craniofacial bones, and tissues of teeth.* Physiologic and pathologic mineral densities of skeletal bones (*Ai*, top row) and their cortical and trabecular compartments (*Aii*, bottom row) and oral and craniofacial tissues (*B*) are shown. MD measurements reported in milligrams of mineral per unit of cubic centimeter (mg/cc) (*Bi*, top row) and Hounsfield units (*Bii*, bottom row) are shown. All graphs contain horizontal lines (colored) that are scaled to the mineral densities of calibration specimens. * indicate significant differences ($P < 0.05$).

a higher MD (504–1009 mg/cc) compared to trabecular bone (82–212 mg/cc) (Fig. 2**Ai–ii**). Tissues of teeth, including enamel, dentin, and cementum illustrated the highest mineral densities (Fig. 2**Bi**) compared to skeletal bones. Both skeletal bone and craniofacial tissues illustrated significant overlaps in average mineral densities between physiologic and pathologic biominerals (Fig. 2**A and B**). Note that the units in Fig. 2**Bii** are presented in HU (y-axis) but are presented relative to mg/cc (lines of different colors illustrate a scale in mg/cc).

3.2. *Calibration of CBCT and micro-CT gray scale values to mg/cc using segments of known shapes and sizes, and mineral densities (Fig. 3)*

Calibration specimens consisting of segments of known mineral densities (MD) in mg/cc were scanned using CBCT and micro-CT systems (Fig. 3**A**). Distinct delineations between each gray value ranging from 0 to 750 mg/cc was observed with the micro-CT which was apparent at both 40 kVp and 90 kVp scanning voltage. The gray scale distinctions, however, were not discernible using the CBCT systems-instead a smooth transition from lower to higher gray values was observed (Fig. 3**Bii**). Scanning parameters influenced gray value to HU conversion, but this difference was minimal for HU to mg/cc conversion (Fig. 3**Bii–iii**).

3.3. *Length-scale characterization of craniofacial specimens (Fig. 4) and ectopic biominerals (Fig. 5)*

As expected, the mineral densities (mean ± SD mg/cc) of enamel (1806 ± 330 mg/cc), dentin (778 ± 147 mg/cc), and cortical (693 ± 197 mg/cc) and trabecular (332 ± 143 mg/cc) bones were significantly different ($P < 0.05$; Fig. 4**A**). The 3D

A. X-ray CT scanning parameters

i. CBCT

Cone Bean Computed Tomography

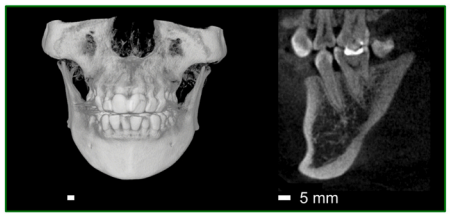

	CBCT 1	CBCT 2
Type	Carestream CBCT CS 9300	Carestream CBCT CS 8100
Field of view	11cm x 17cm	8cm x 9cm
Voxel size	250µm x 250µm x 250µm	150µm x 150µm x 150µm
Current	4 mA	4 mA
Voltage	90 kVp	84 kVp
Absorbed dose (dose area product) *	897 mGy.cm²	1169 mGy.cm²
Effective dose *	~0.142 mSv	~0.045 mSv

* from manufacturer

ii. Micro-XCT

Micro X-ray Computed Tomography

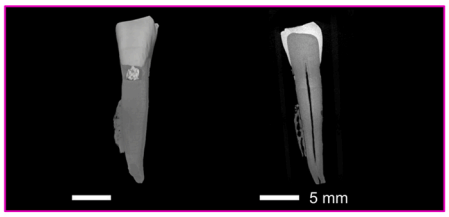

	Micro-XCT 1	MicroXCT 2
Type	Zeiss MicroXCT-200 (4X)	Zeiss MicroXCT-200 (4X)
Field of view	0.5cm x 0.5cm	0.5cm x 0.5cm
Voxel size	5µm x 5µm x 5µm	5µm x 5µm x 5µm
Current	0.198 mA	0.088 mA
Voltage	40 kVp	90 kVp
Absorbed dose (dose area product) **	210 mGy.cm²	470 mGy.cm²
Effective dose	-	-

** calculated from Current and Voltage

$D = Wfat/4\pi r^2$, $f = 10^{-6}EZ$

Where W: power (ergs/sec), E: electron energy (keV), Z: atomic number, a: mass energy absorption coefficient (cm²/g), t: exposure time (sec), r: sample to source distance (cm).

B. CBCT and Micro-XCT calibration

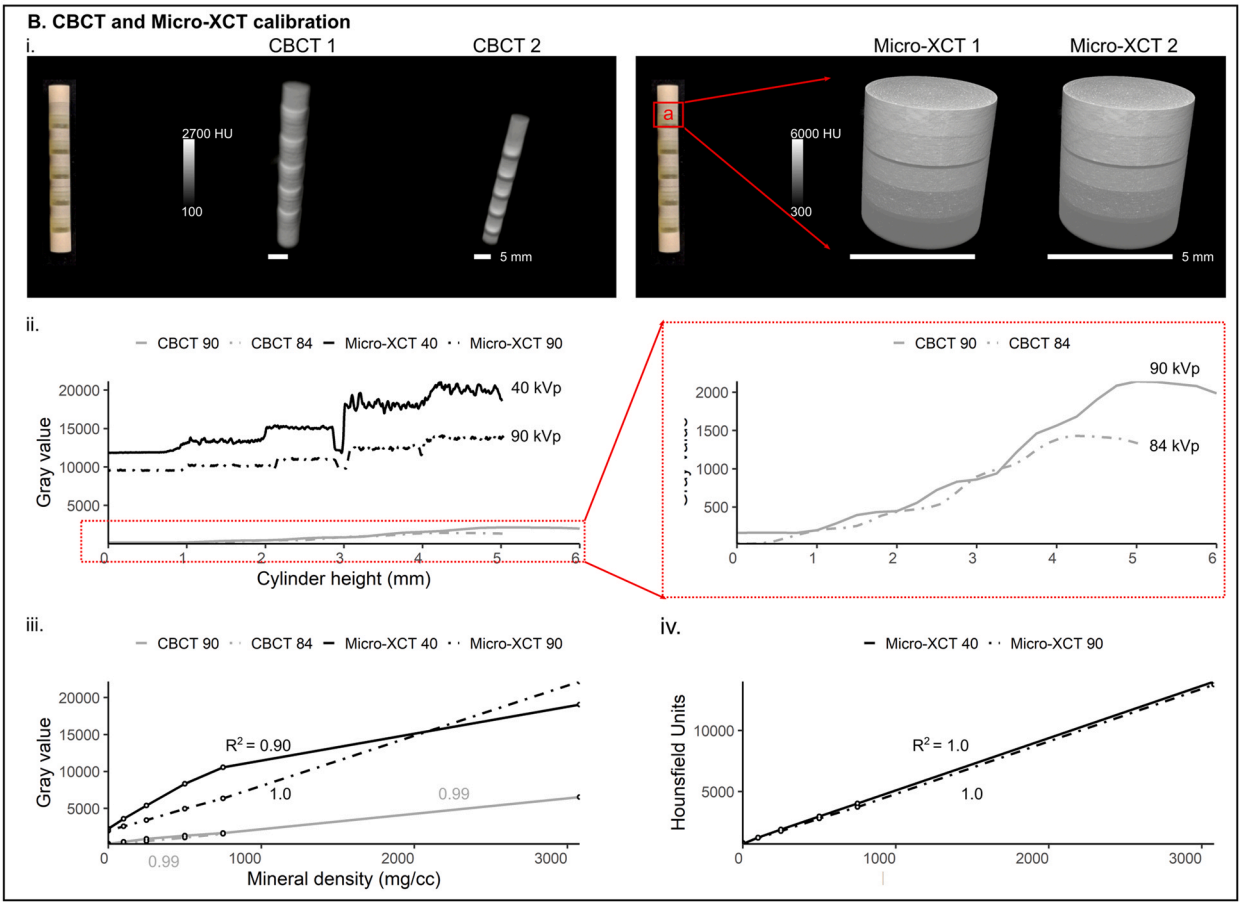

Fig. 3 – *Calibration of CBCT and micro-CT using standards of known mineral densities.* (A) Representative CBCT and micro-CT scans (*Ai and ii*), scanning parameters of CBCT and micro-CT (*Ai-ii*), and calibration standard with segments of uniform width and known MD ranging from 0 to 750 mg/cc (*Bi*) are shown. (*B*) Calibration curves for the respective CT systems are obtained

by extracting the gray value profile along the length of the calibration standard (red box *(B, a; B, i)*). Line profiles *(Bii)* of gray values to evaluate resolution capacity of density from all scanners are illustrated. Gray values are correlated with mineral densities *(Biii)* of the segments to generate calibration curves for CT systems respectively. The correlation between Hounsfield units.vs. mineral densities *(Biv)* of micro CT also is shown.

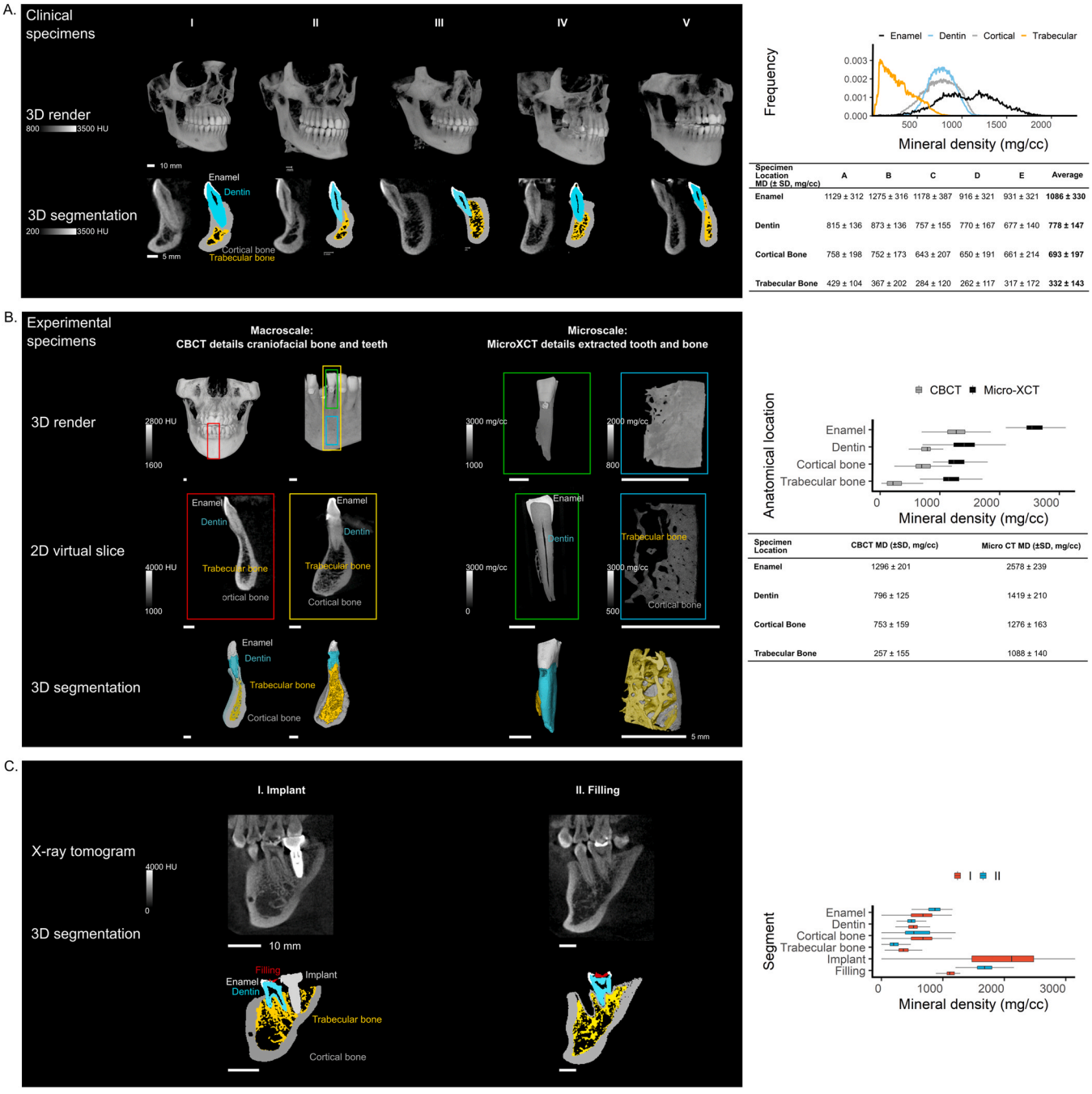

Specimen Location MD (± SD, mg/cc)	A	B	C	D	E	Average
Enamel	1129 ± 312	1275 ± 316	1178 ± 387	916 ± 321	931 ± 321	**1086 ± 330**
Dentin	815 ± 136	873 ± 136	757 ± 155	770 ± 167	677 ± 140	**778 ± 147**
Cortical Bone	758 ± 198	752 ± 173	643 ± 207	650 ± 191	661 ± 214	**693 ± 197**
Trabecular Bone	429 ± 104	367 ± 202	284 ± 120	262 ± 117	317 ± 172	**332 ± 143**

Specimen Location	CBCT MD (±SD, mg/cc)	Micro CT MD (±SD, mg/cc)
Enamel	1296 ± 201	2578 ± 239
Dentin	796 ± 125	1419 ± 210
Cortical Bone	753 ± 159	1276 ± 163
Trabecular Bone	257 ± 155	1088 ± 140

Fig. 4 – *Estimated mineral densities of human craniofacial bones and dental tissues are length-scale dependent.* (A) Rendered volumes of human dental and craniofacial tissues as seen by the CBCT illustrate apparent differences and ranges in gray scale intensities (histograms, table) between enamel, dentin, and cortical and trabecular bones. (B) 3D rendered volumes of enamel, dentin, and cortical and trabecular bones as seen by CBCT and micro-CT systems, and intensity-based segmentation illustrate higher MD values of dental tissues (box plots, table) by micro-CT compared to CBCT. Note: enamel (white), dentin (turquoise), cortical (grey) and trabecular (yellow) bones. (C) Mandibular jaw with a dental implant, tooth-filling, and surrounding cortical and trabecular bones of varying mineral densities (box plots) are shown.

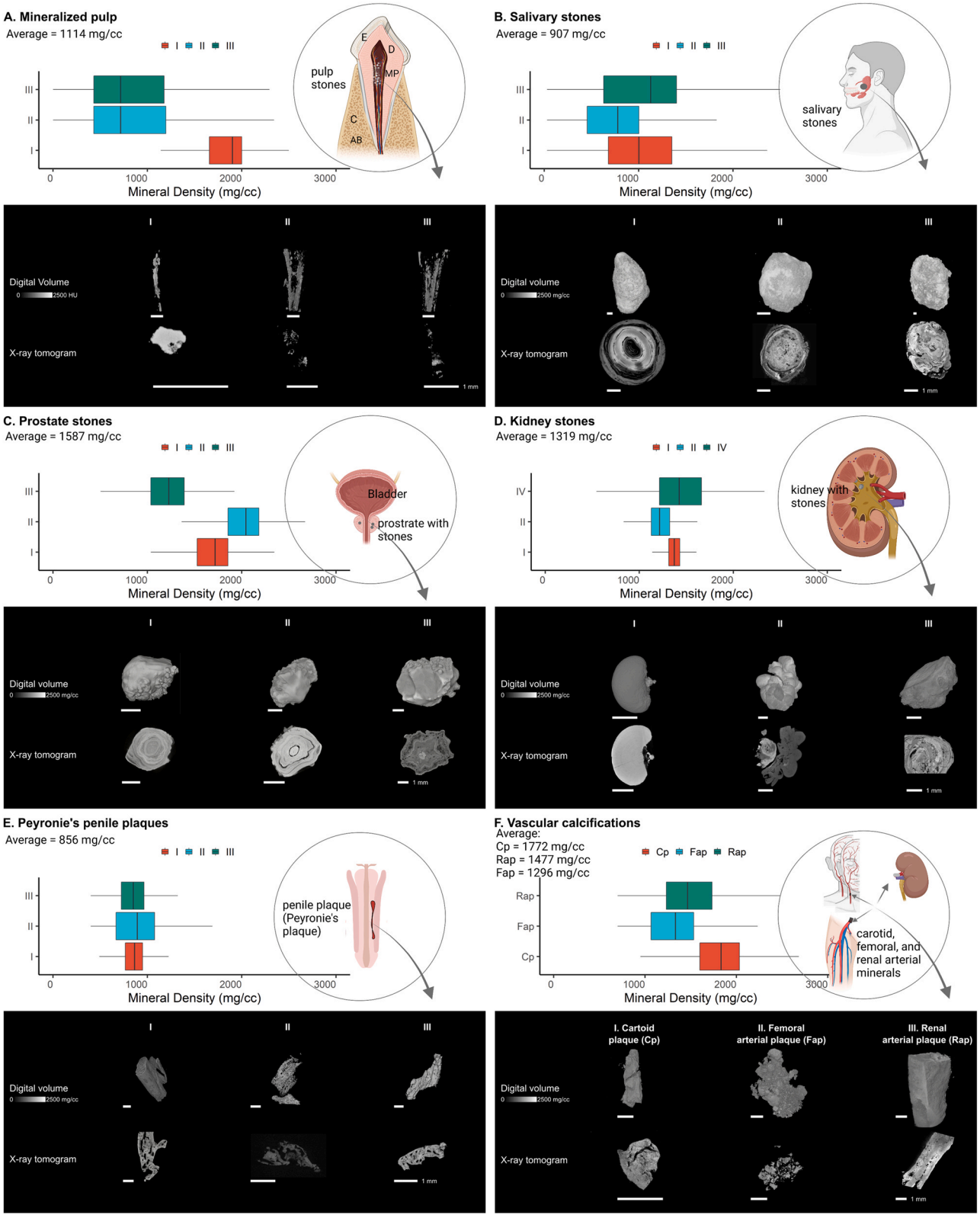

Fig. 5 – *Mineral densities and structural heterogeneities within pulp, salivary, prostate, and kidney stones, and renal, penile and vascular plaques.* Rendered volumes (top row), virtual sections (bottom row), and ranges in mineral densities (box plots) of ectopic biominerals including (*A*) mineralized pulp, (*B*) salivary (*C*) prostate and (*D*) kidney stones, and (*E*) Peyronie's penile, (*F*) carotid, femoral arterial, and renal arterial plaques are shown.

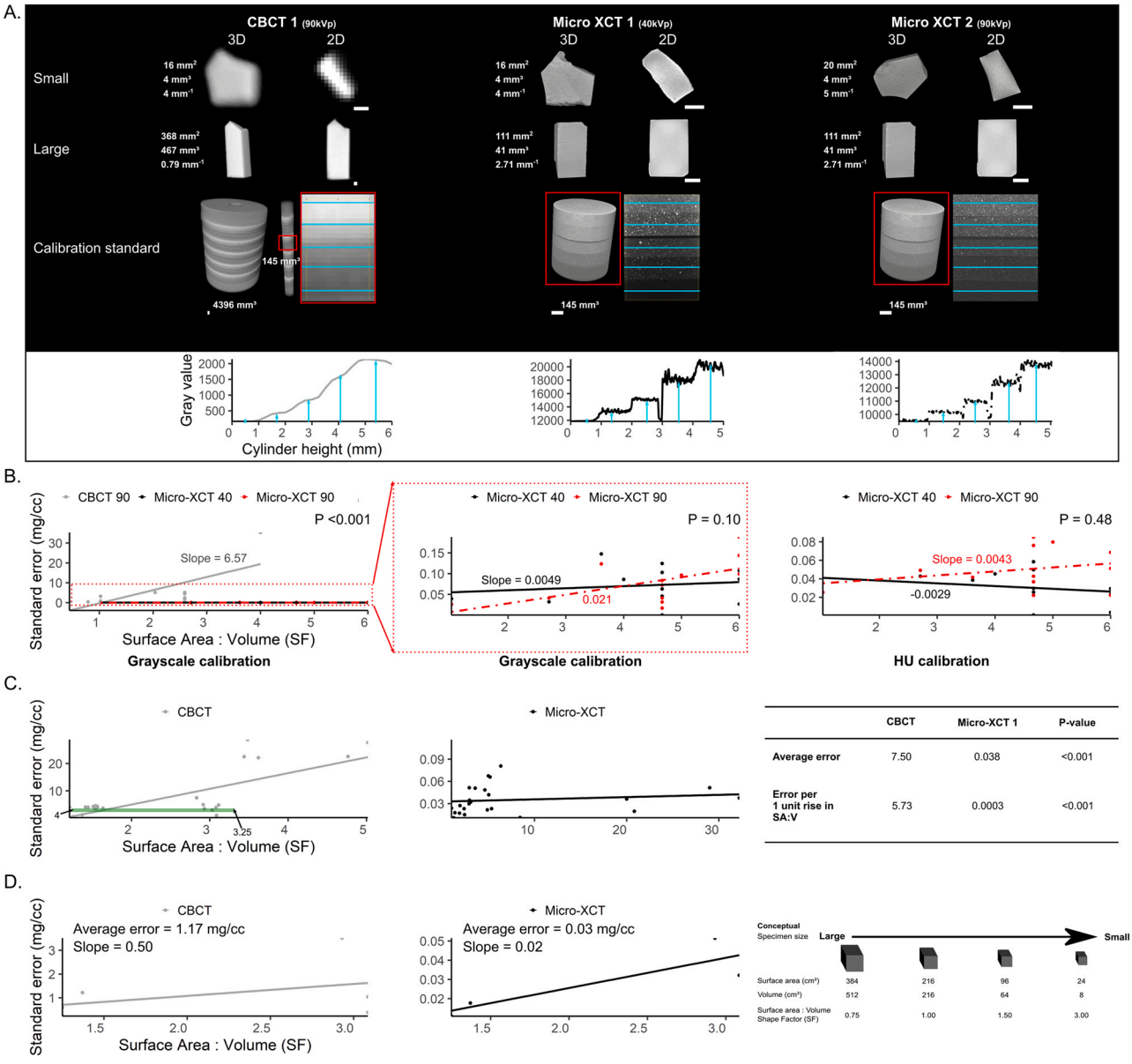

	CBCT	Micro-XCT 1	P-value
Average error	7.50	0.038	<0.001
Error per 1 unit rise in SA:V	5.73	0.0003	<0.001

Fig. 6 – *Calculated error in MD estimates of specimens are related to shape factor of an object.* (A) Rendered volumes and tomograms of hydroxyapatite specimens of different sizes and shapes, and gray value profiles along the thickness of the specimens using CBCT and micro-CT units. (B) Calculated error (standard error) in MD estimates vs. surface area to volume ratio (shape factor; SF) of calibration specimens in CBCT and micro-CT units (solid line, linear fit; dotted line, locally estimated scatter plot smoothing [LOESS] fit) are shown. (C) Error in MD estimates of experimental specimens as a function of SF are shown along with slopes of change in error (table). (D) Error in MD estimates when scanning the same dental tissues using both scanners are shown. Note: standard error = standard deviation/√ sample size.

rendered volume and 2D virtual slices illustrated differences in voxel and pixel spatial resolutions of the craniofacial and dental tissues when using the CBCT and micro-CT scanners respectively (Fig. 4). Further segmentation of the same dental tissues and craniofacial bones, and measurements of mineral densities demonstrated consistently lower estimates of MD in CBCT compared to micro-CT. For example, enamel showed MD of (1296 ± 201 mg/cc) when scanned using a CBCT vs. (2578 ± 239 mg/cc) when scanned using a micro-CT; both scanners were calibrated with the same standard (Fig. 4**B**). Inherent structural differences in ectopic biominerals using micro-CT, as well as inter- and intra-specimen heterogeneities in tissues of the teeth, and salivary, prostate, and kidney stones, and penile and vascular plaques (Fig. 5) were observed.

3.4. *The effect of shape-factor and error in measured mineral densities (Fig. 6)*

Gradients of gray scale were observed by scanning hydroxyapatite (HA) specimens of varying sizes (volume: 4–467 mm^3, shape-factor: 0.79–5 mm^{-1}) and calibration standards containing HA particulates within segments of known mineral densities using CBCT. Distinct differences between zones of gray values in addition to HA particulates within each segment, were visible, but only with micro-CT (Fig. 6**A**). Measurement error quantified as standard error of mean MD showed error dependence on size of the scanned specimen. CBCT, on average, showed 6.6 mg/cc increase in error per unit increase in surface-area to volume ratio ($P < 0.001$). No significant difference in error related to size (SA:V) of the specimen was observed when scanned using micro-CT under 40 kVp and 90 kVp (Fig. 6**B**). When quantifying error dependence of MD on phantom size using calibration standards and experimental specimens, micro-CT showed little to no dependence (slope: 0.0003 mg/cc per unit chance in SA:V), whereas, CBCT showed a significantly positive correlation (slope: 5.7 mg/cc per unit change in SA:V) such that as the size of the specimen decreased (increase in shape-factor), an increase in measurement error of MD was observed (Fig. 6**C**). Specimens within a range of 0.79–3.25 mm^{-1} (SA:V) and within a spatial resolution of at least 0.42 mm^3 (based on voxel size of 250 µm) showed minimal change in measured MD error ($\pm$ 4 mg/cc). This trend of increased error with increasing shape-factor persisted when scanning the same dental tissues using both CBCT scanners (Fig. 6**D**).

3.5. *Atlas of physiologic and pathologic mineral densities of biominerals (Fig. 7)*

Estimates of pooled mineral densities extracted from the meta data-analysis (Fig. 1) and weighted by the number of patients illustrated significant differences between physiologic and pathologic MD (mg/cc) in the cortical compartment of lumbar vertebral bodies, radius and tibia, and the trabecular compartment of radius and tibia (Fig. 7**B**). Cementum of craniofacial and dental tissues, also differed significantly (Fig. 7**A**). Map of MDs from meta-analysis supplemented with those of pathologic biominerals scanned at a higher resolution (voxel size: 5 µm) showed varying degrees of overlap between tissue types (Fig. 7**C**).

4. Discussion

Reliable detection of acute and chronic disease states using radiographic imaging with the goal of mitigating disease progression remains a challenge. Meta-analysis on mineral densities within the literature (Fig. 1) illustrated no significant patterns that could delineate group-specific physiologic and pathologic average mineral densities (Fig. 2). The primary effectors for the observed overlap may be the use of different scanners (Fig. 3), and the lack of a calibrated X-ray imaging protocol *in vivo* [6,7,14]. Regardless of these limitations, macro-trends such as clustering of cortical and trabecular bone into higher and lower MD ranges, respectively, were observed (Fig. 2**B**).

In a radiograph, the differences in gray scales between pixels (2D) or voxels (3D) are exploited to identify abnormalities in mineralized tissues. Intensities that are reflective of absorbed dose are normally reported as gray scale but in arbitrary units (a.u.) [14]. Arbitrary units are scaled to Hounsfield units (HU), and on occasion are translated to milligrams per unit volume usually in centimeter cube (mg/cc) [15]. Gray shades, fundamentally are an estimate of the mineral densities of a physical mass/matter [16,17]. Clinical X-ray detectors, however, are often calibrated to – 1000 HU for air and 0 HU for water [18]. Given this narrow range, the use of HU to differentiate a wide range of pathologies from fatty liver to osteoporosis is improbable [3,4,19]. The current practice involves fitting intensity based gray values to HU ranges of air and water under the assumption that most scanner-to-detector relationships are linear, and that this relationship is independent of source power. This confounding factor of the covariance in source power to absorbed dose by the specimen scanners could affect MD measurements regardless of their anatomical locations [14,20]. Furthermore, it is conceivable that the absence of standardization could be yet another plausible explanation for the observed overlap between physiologic and pathologic MDs (Fig. 2). For these reasons imaging *in vivo* through the use of phantoms with known mineral densities will provide spatial maps of pathologic biominerals, but within the confines of the spatial resolution of CT scanners, resulting in unreliable measures.

Spatiotemporal sensitivity of a scanner to structural and MD changes within tissues/organs will guide a physician to detect risk and disease burden [21–23]. Reliable detection of disease burden is dependent on the size and shape of the pathology [24–26]. Acute and chronic changes in pathologies should be detected both as a change in shape and MD, or a combined effect of the two. In addition to gray scale to mg/cc conversion/calibration of CT scanners, there lies yet another challenge in that the spatial resolving capacities of clinical scanners also should be challenged. This brings to light yet another limitation, in that, the scanner's resolution also should be adequate to detect spatiotemporal structural changes in pathologic biominerals.

The visually apparent spatial resolution discrepancies of the same specimens by CBCT and micro-CT scanners (Figs. 4, 5) illustrated the need for spatial sensitivity and spatial calibration of the CBCT scanner; that is calibration should not be limited to MD alone (Figs. 4**B**, 6). The variation in MD (Fig. 4**B**) revealed that the intensity differences also are based on structure of the same matter/pathology and is length-scale specific. Micron-sized finer particulates within the larger segments, were detailed by micro-CT (Fig. 6**A**, micro-CT scans), and were not seen by the CBCT. These apparent differences in length scales across the systems also delineate scanner-specific spatial resolutions. Given that the intrinsic MD measures are size and scanner specific, a safe operating spatial zone for CBCT was identified with a shape-factor range of 0.79–3.25 mm^{-1} that permits on an average $\pm$ 4 mg/cc error in measurement (Fig. 6**C and D**), and specimens and

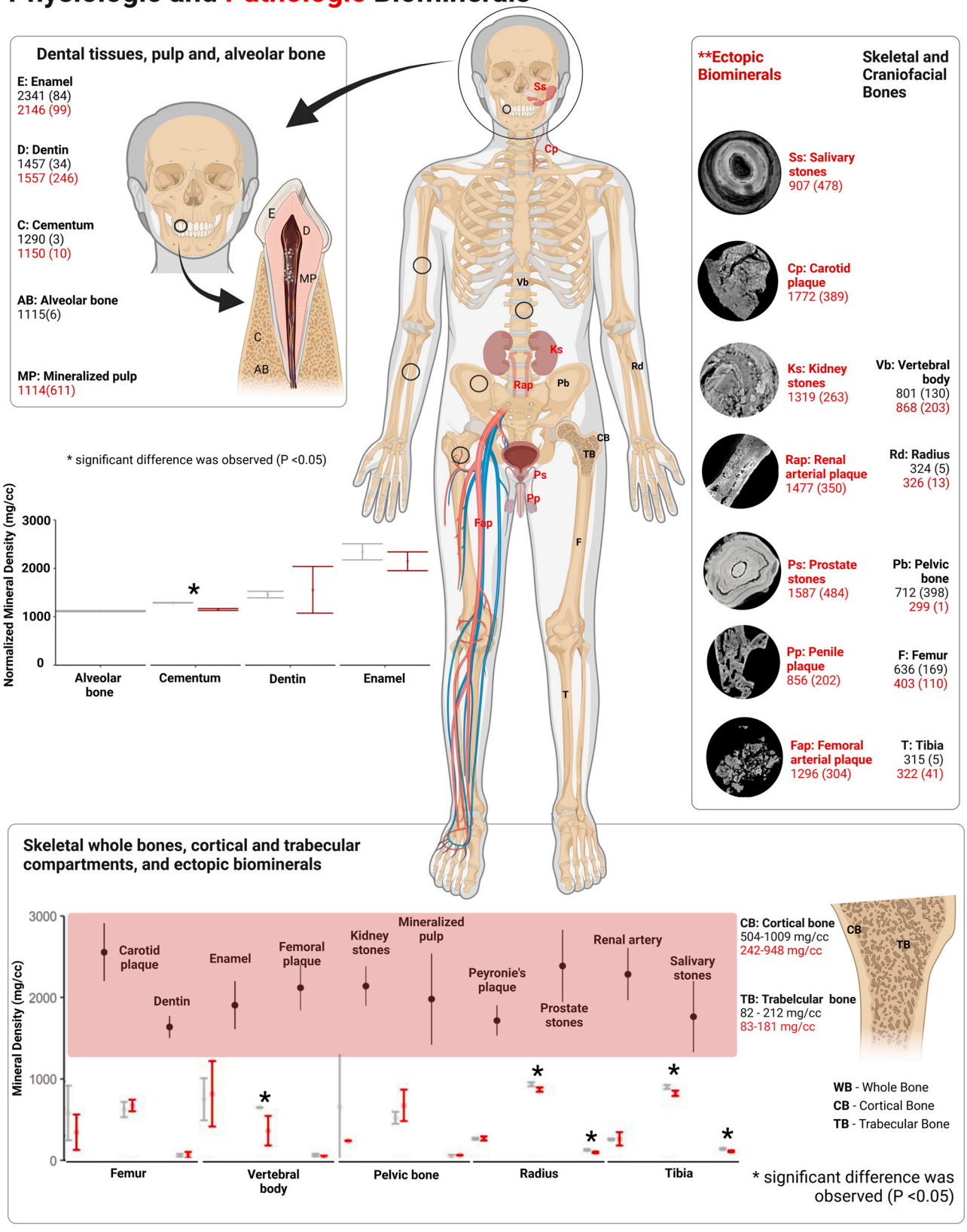
Physiologic and Pathologic Biominerals
Dental tissues, pulp and, alveolar bone
E: Enamel
2341 (84)
2146 (99)
D: Dentin
1457 (34)
1557 (246)
C: Cementum
1290 (3)
1150 (10)
AB: Alveolar bone
1115(6)
MP: Mineralized pulp
1114(611)
E
D
MP
C
AB
* significant difference was observed (P <0.05)
Normalized Mineral Density (mg/cc)
3000
2000
1000
0
Alveolar bone
Cementum
Dentin
Enamel
**Ectopic Biominerals
Skeletal and Craniofacial Bones
Ss: Salivary stones
907 (478)
Cp: Carotid plaque
1772 (389)
Ks: Kidney stones
1319 (263)
Rap: Renal arterial plaque
1477 (350)
Ps: Prostate stones
1587 (484)
Pp: Penile plaque
856 (202)
Fap: Femoral arterial plaque
1296 (304)
Vb: Vertebral body
801 (130)
868 (203)
Rd: Radius
324 (5)
326 (13)
Pb: Pelvic bone
712 (398)
299 (1)
F: Femur
636 (169)
403 (110)
T: Tibia
315 (5)
322 (41)
Ss
Cp
Vb
Ks
Rd
Rap
Pb
CB
TB
Ps
Pp
Fap
F
T
Skeletal whole bones, cortical and trabecular compartments, and ectopic biominerals
Mineral Density (mg/cc)
3000
2000
1000
0
Carotid plaque
Dentin
Enamel
Femoral plaque
Kidney stones
Mineralized pulp
Peyronie's plaque
Prostate stones
Renal artery
Salivary stones
Femur
Vertebral body
Pelvic bone
Radius
Tibia
CB: Cortical bone
504-1009 mg/cc
242-948 mg/cc
TB: Trabelcular bone
82 - 212 mg/cc
83-181 mg/cc
CB
TB
WB - Whole Bone
CB - Cortical Bone
TB - Trabecular Bone
* significant difference was observed (P <0.05)

Fig. 7 – *Atlas on MD ranges of various physiologic and pathologic tissues in a human body*. Meta data (plots) of mineral densities of physiologic and pathologic tissues from literature; and their 95% confidence interval and average MDs of cortical, trabecular and their collective averages are shown. Physiologic and pathologic tissues including the lumbar spine, cortical and trabecular compartments of radius and tibia illustrate no overlap in respective MD ranges (*Aii*, see asterisks). No overlap in MDs of physiologic and pathologic cementum (*Bii*, see asterisks) was observed. MDs and their respective standard deviation of specimens from literature and specimens scanned using micro-CT (see asterisks) are shown. Ranges of MDs within the human body, based on meta-analysis, along with mineral densities of their cortical and trabecular compartments are illustrated (bottom row).

sizes above the upper threshold will render an increased error in reader's interpretation.

The beginnings of a pathology are often smaller 4-5 μm in size (routine CT spatial resolution range 5 - 400 μm), and are not detectable with current CT systems. Often, the size of a lesion also is used as a measure for disease prognosis [27,28]. Semi-quantitative maps of breast calcifications that include number, size, and shades of radiolucency, for example illustrated that CT calibration should not be limited to density only, but should also include its spatial dimensions [27,29]; the surface area to volume ratio of a specimen or its shape-factor (Fig. 6). In essence, calibration of CT scanners for shape-factor effect on MD will minimize specimen size-specific error, and increase the disease prognosis accuracy. The error in MD measurements increases in CT systems that are only calibrated for MD without accounting for shape of the unit volume of mineral (Fig. 6**C**). Proposed calibration for an accurate disease detection and prognosis therefore should include MD vs. specimen shape-factor. Results of this study proposed insights into the use of calibration standards with segments of defined geometries and known MDs (Fig. 6). This systematic approach using calibration standards would allow conversion of grey scale to the absorbed dose by each segment with a known shape-factor and MD. This approach would be akin to calibrating a mechanical testing equipment to known strengths of various standard materials with defined geometry as per the guidelines of American Standards for Testing Materials (ASTM) [30,31].

The current state of radiographic technology that exploits daily and weekly calibration is best expressed through high-resolution peripheral quantitative computed tomography (HR-pQCT; 9.4–68 kVp and 0.9–1.5 mA) that demonstrates calibrated but short-term single-site precision [32,33]. Calibrated approach used in HR-pQCT enables higher resolution (voxel size of 61–82 μm) quantitative maps of bone structure and MD of peripheral tissues; a systematic approach with HR-pQCT is already in use by the clinics. A similar approach should be encouraged when using CBCT and whole-body CT in clinics to generate calibrated scans of patients, with an end goal of generating quantitative and reliable MD maps as clinicians follow their patients. Such standardization protocol would aid in generalization of CBCT scanning despite knowing that variation in scanning parameters and scanner types can expose patients to a wide range X-ray energies [34]. Based on this systematic study, a detectable net difference of at least 50 mg/cc (physiologic - pathologic mineral densities) regardless of the scanner resolution is proposed as an early-stage indicator of pathologic biomineralization (Fig. 7).

A two-step standardization protocol to generate spatio-temporal quantitative evaluations of pathologies *in vivo* is proposed. Steps include **1)** calibrate scanners with standards containing segments of known geometries (**Step 1,** Fig. 8) and MDs; **2)** scan patients with a calibration specimen to establish a quantitative and a reliable spatial map of MDs accurate to both size and shape (**Step 2,** Fig. 8). The first step would permit identification of upper and lower threshold limits of the scanner, and will allow reliable detection of MD based on size and X-ray attenuation. The second step will map and confirm the mineral densities of scanned mineralized tissues (physiologic and pathologic) *in vivo*. The transition of standard calibration from gray value and HU to mg/cc using phantoms of known MDs and shapes, and known scanning conditions would permit *in vivo* spatiotemporal quantitative evaluations of pathologies albeit the resolution being length-scale dependent.

5. Limitations and Conclusions

The observable minimum error in measured MD using a micro-CT was because of a narrow range of SA:V ratio. Similar to the CBCT that was used for scanning macro-meter to micro-meter sized specimens, the micro-CT should be challenged from micro-meter to nano-meter sized specimens to estimate the effect of shape-factor on vs. standard error in MD measurements. The existing literature does not clearly delineate the differences in physiologic and pathologic mineral densities. Based on this systematic study a detectable net difference of at least 50 mg/cc (physiologic - pathologic mineral densities) regardless of the scanner resolution is proposed as an early-stage indicator of pathologic biomineralization (Fig. 7). Reliable detection of net changes in mineral densities and feature sizes is required for tracking spatio-temporal changes in pathologic tissues.

The outcomes from this study within the context of the aforementioned objectives are as follows. **1)** Meta-analysis of the data from literature identified larger macro-trends in MD differences (cortical bone vs. trabecular bone), but failed to consistently delineate pathologic from physiologic mineral densities. **2)** Calibrated quantitative MD maps underscored the effects of "feature shape and size" on MD. **3)** This systematic study underpinned the "information gap" by highlighting the "safe-operating zones" across length-scales (CBCT and micro-CT). Based on this systematic study, a detectable net difference of at least 50 mg/cc (physiologic - pathologic mineral densities) regardless of scanner resolution is

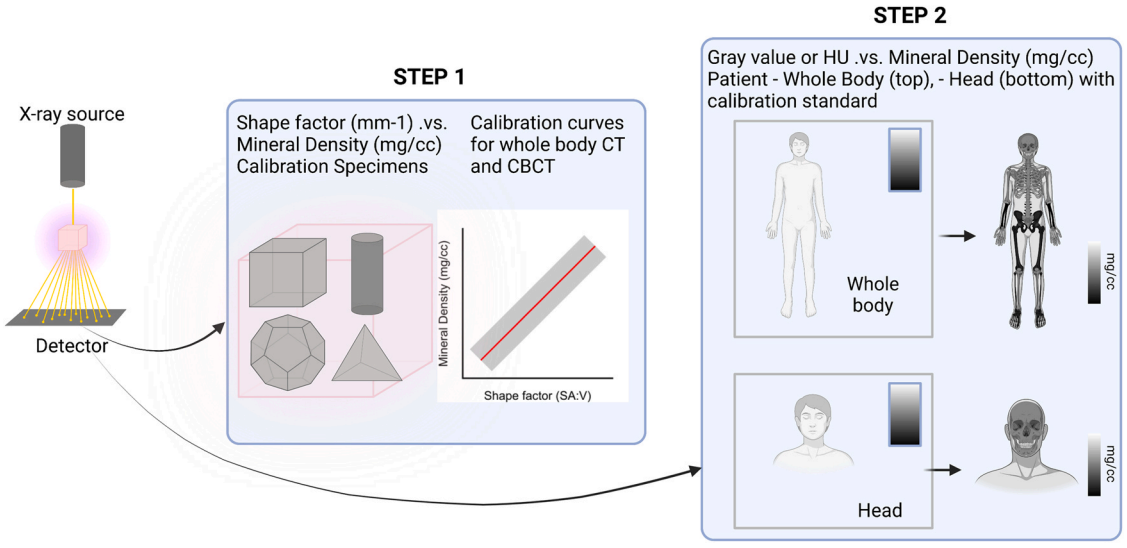

Fig. 8 – *Standardization of CT imaging in vivo across length-scales*. Standardization of CT imaging across length-scales can provide insights into pathophysiology by mapping, the MD, and structure of biominerals. A two-step calibration method includes scanning calibration specimens of *1)* different shapes and sizes, with different mineral densities to generate necessary scanner calibration curves; *2)* scan patient's whole body and head using the same calibration specimens identified in step 1.

proposed as an early-stage indicator of pathologic biomineralization (Fig. 7). Reliable detection of net changes in MDs and feature sizes is required for tracking spatiotemporal changes in pathologic tissues. **4)** the practical utility of this study lies within the proposed standardization protocol to decrease the error in reader's interpretation of CT scans. Future studies and manufacturers should calibrate scanners using phantoms of different sizes and shapes to generate shape-factor vs. MD calibration curve that would decrease the error in reader's interpretation and clinical diagnosis. Lastly, **5)** Correlative microspectroscopic approaches that also interface with radiographic CT scanners are needed to investigate the root cause of biomineralization. For example, tumor malignancy with single photon emission computed tomography (SPECT) is complemented with radiographic CT to allow macroscale spatial visualization of the tumor. Similarly, year-long chemotherapies can be paired with calibrated CT evaluation to monitor bone response to chemotoxins to visualize the emergence of collateral damage to prevent long-term fracture risk.

While no one system can aid in visualization of a complex pathophysiological process that results in pathologic biominerals (Figs. 5, 7); investigation of "root" cause of biomineralization will benefit from correlative approaches that also interface with radiographic CT scanners. For example, just as tumor malignancy with single photon emission computed tomography (SPECT) is complemented with radiographic CT to allow macro-scale spatial visualization of the tumor, year-long chemotherapies can be paired with calibrated CT evaluation to monitor bone response to chemotoxins to visualize the emergence of collateral damage to prevent long-term fracture risk .

Funding

This research was funded by the Program in Biomineralization Studies (PiBiomS), Departments of Preventive and Restorative Dental Sciences, and Urology, Schools of Dentistry and Medicine, University of California San Francisco, California, USA. PiBiomS is a program built on the partnership between the Schools of Dentistry and Medicine at UCSF to investigate the pathophysiology of ectopic biominerals in humans.

Credit authorship contribution statement

S. Srirangapatanam contributed to data acquisition, analysis, and interpretation, and drafted the manuscript; **M. Kang**, contributed to design, data acquisition, analysis, and interpretation but was specific to craniofacial scans, and micro CT related scans; **Y. Ellenikiotis**, contributed to quantitative measurements of craniofacial and dental tissue scans, and interpretation of CBCT and micro CT data; **A. Jheon, S. Kapila, H. Swana, M. Stoller**, and **Y. Seo** contributed the practical interpretation of data within the realm of current state of the art X-ray technology, and the need for a systematic approach that would drive a reliable measure for an effective patient-care. **S. Ho** contributed to study design, data analysis, interpretation, and science, edited, revised and critically reviewed the manuscript with all authors. All authors gave final approval and agree to be accountable for all aspects of the work.

Data Availability Statement

The data that support the findings of this study are available on request from the corresponding author. The data are not publicly available due to privacy or ethical restrictions.

Acknowledgements

The authors thank M. Ferrar for her help in developing the calibration standards, and manufacturing them in collaboration with CRIS. The authors thank N. Foreman, A. Raymundo, O. Almaghafi for their help in collecting data from the PubMed database for meta-analysis. The authors thank the Biomaterials and Bioengineering Correlative Microscopy Core, University of California San Francisco, for use of the MicroXCT-200 to scan ectopic biominerals from humans. Figs. 2, 5, 7, and 8 were partially generated using BioRender.com.

Appendix A. Supporting information

Supplementary data associated with this article can be found in the online version at doi:10.1016/j.dental.2022.03.010.

REFERENCES

[1] Kawasaki K, Buchanan AV, Weiss KM. Biomineralization in humans: making the hard choices in life. Annu Rev Genet 2009;43:119–42. https://doi.org/10.1146/annurev-genet-102108-134242
[2] Rubin GD. Emerging and evolving roles for CT in screening for coronary heart disease. J Am Coll Radiol 2013;10(12):943–8. https://doi.org/10.1016/j.jacr.2013.09.018
[3] Zeb I, Li D, Nasir K, Katz R, Larijani VN, Budoff MJ. Computed tomography scans in the evaluation of fatty liver disease in a population based study: the multi-ethnic study of atherosclerosis. Acad Radiol 2012;19(7):811–8. https://doi.org/10.1016/j.acra.2012.02.022
[4] Narayanan A, Cai A, Xi Y, Maalouf NM, Rubin C, Chhabra A. CT bone density analysis of low-impact proximal femur fractures using Hounsfield units. Clin Imaging 2019;57:15–20. https://doi.org/10.1016/j.clinimag.2019.04.009
[5] Merrett SJ, Drage NA, Durning P. Cone beam computed tomography: a useful tool in orthodontic diagnosis and treatment planning. J Orthod 2009;36(3):202–10. https://doi.org/10.1179/14653120723193
[6] Cannillo B, Ostan A, Dionisi C, Fusco G, Carriero A, Brambilla M. Variability of the discrepancy between manufacturer and measured CTDI100 values by scanner type, acquisition parameters and phantom size. Phys Med 2018;49:34–9. https://doi.org/10.1016/j.ejmp.2018.04.390
[7] Mackin D, Fave X, Zhang L, Fried D, Yang J, Taylor B. Measuring computed tomography scanner variability of radiomics features. Invest Radiol 2015;50(11):757–65. https://doi.org/10.1097/RLI.0000000000000180.
[8] Oh JH, Choi SP, Wee JH, Park JH. Inter-scanner variability in Hounsfield unit measured by CT of the brain and effect on gray-to-white matter ratio. Am J Emerg Med 2019;37(4):680–4. https://doi.org/10.1016/j.ajem.2018.07.016
[9] Symons R, Morris JZ, Wu CO, Pourmorteza A, Ahlman MA, Lima JA. Coronary CT angiography: variability of CT scanners and readers in measurement of plaque volume. Radiology 2016;281(3):737–48. https://doi.org/10.1148/radiol.2016161670.
[10] Williams MC, Newby DE. CT myocardial perfusion imaging: current status and future directions. Clin Radiol 2016;71(8):739–49. https://doi.org/10.1016/j.crad.2016.03.006
[11] Schröder L, Stankovic U, Sonke JJ. Technical note: long-term stability of Hounsfield unit calibration for cone beam computed tomography. Med Phys 2020;47(4):1640–4. https://doi.org/10.1002/mp.14015
[12] R Core Team. R: a language and environment for statistical computing. Vienna, Austria: R Foundation for Statistical Computing; 2021⟨https://www.R-project.org/⟩.
[13] Viechtbauer W. Conducting meta-analyses in R with the metafor package. J Stat Softw 2010;36(3):1–48⟨https://www.jstatsoft.org/v36/i03/⟩.
[14] Levi C, Gray JE, McCullough EC, Hattery RR. The unreliability of CT numbers as absolute values. AJR Am J Roentgenol 1982;139(3):443–7. https://doi.org/10.2214/ajr.139.3.443
[15] Razi T, Niknami M, Alavi Ghazani F. Relationship between Hounsfield unit in CT scan and Gray scale in CBCT. J Dent Res Dent Clin Dent Prospects 2014;8(2):107–10. https://doi.org/10.5681/joddd.2014.019
[16] Kinney JH, Nichols MC. X-ray tomographic microscopy (XTM) using synchrotron radiation. Annu Rev Mater Sci 1992;22(1):121–52.
[17] Mazonakis M, Damilakis J. Computed tomography: what and how does it measure? Eur J Radiol 2016;85(8):1499–504. https://doi.org/10.1016/j.ejrad.2016.03.002
[18] Mah P, Reeves TE, McDavid WD. Deriving Hounsfield units using grey levels in cone beam computed tomography. Dentomaxillofac Radiol 2010;39(6):323–35. https://doi.org/10.1259/dmfr/19603304
[19] Gausden EB, Nwachukwu BU, Schreiber JJ, Lorich DG, Lane JM. Opportunistic use of CT imaging for osteoporosis screening and bone density assessment: a qualitative systematic review. J Bone Jt Surg Am 2017;99(18):1580–90. https://doi.org/10.2106/JBJS.16.00749
[20] Bolus D, Morgan D, Berland L. Effective use of the Hounsfield unit in the age of variable energy CT. Abdom Radiol 2017;42(3):766–71. https://doi.org/10.1007/s00261-017-1052-4
[21] Nakasu S, Onishi T, Kitahara S, Oowaki H, Matsumura KI. CT Hounsfield unit is a good predictor of growth in meningiomas. Neurol Med Chir 2019;59(2):54–62. https://doi.org/10.2176/nmc.oa.2018-0209
[22] Sabel N. Enamel of primary teeth–morphological and chemical aspects. Swed Dent J Suppl 2012;222. [1-i].
[23] Pereira RC, Bischoff DS, Yamaguchi D, Salusky IB, Wesseling-Perry K. Micro-CT in the assessment of pediatric renal osteodystrophy by bone histomorphometry. Clin J Am Soc Nephrol 2016;11(3):481–7. https://doi.org/10.2215/CJN.04810515
[24] Onishi H, Hori M, Ota T, Nakamoto A, Osuga K, Tatsumi M. Phantom study of in-stent restenosis at high-spatial-resolution CT. Radiology 2018;289(1):255–60. https://doi.org/10.1148/radiol.2018180188.
[25] Lee JH, Cheng KL, Choi YJ, Baek JH. High-resolution imaging of neural anatomy and pathology of the neck. Korean J Radiol 2017;18(1):180–93. https://doi.org/10.3348/kjr.2017.18.1.180
[26] Pena E, Ojiaku M, Inacio JR, Gupta A, Macdonald DB, Shabana W. Can CT and MR shape and textural features differentiate benign versus malignant pleural lesions?. Acad Radiol 2017;24(10):1277–87. https://doi.org/10.1016/j.acra.2017.03.006.
[27] Baldwin P. Breast calcification imaging. Radiol Technol 2013;84(4):383M–408M.
[28] Takashima K, Sakai T, Hamada H, Takao M, Sugano N. Which classification system is most useful for classifying osteonecrosis of the femoral head?. Clin Orthop Relat Res 2018;476(6):1240–9. https://doi.org/10.1007/s11999.0000000000000245

[29] Bassett LW. Mammographic analysis of calcifications. Radiol Clin N Am 1992;30(1):93–105.
[30] ASTM. Standard test method for plane strain fracture toughness of metallic materials. Designation: E399-90. Annual book of ASTM standards vol. 3.01 Philadelphia: American Society for Testing and Materials; 1993.
[31] Creel JA, Stover SM, Martin RB, Fyhrie DP, Hazelwood SJ, Gibeling JC. Compliance calibration for fracture testing of anisotropic biological materials. J Mech Behav Biomed Mater 2009;2(5):571–8. https://doi.org/10.1016/j.jmbbm.2008.11.005
[32] Whittier DE, Boyd SK, Burghardt AJ, Paccou J, Ghasem-Zadeh A, Chapurlat R. Guidelines for the assessment of bone density and microarchitecture in vivo using high-resolution peripheral quantitative computed tomography. Osteoporos Int 2020;31(9):1607–27. https://doi.org/10.1007/s00198-020-05438-5.
[33] Mikolajewicz N, Zimmermann EA, Rummler M, Hosseinitabatabaei S, Julien C, Glorieux FH. Multisite longitudinal calibration of HR-pQCT scanners and precision in osteogenesis imperfecta. Bone 2021;147:115880https://doi.org/10.1016/j.bone.2021.115880.
[34] Ludlow JB, Timothy R, Walker C, Hunter R, Benavides E, Samuelson DB. Effective dose of dental CBCT-a meta analysis of published data and additional data for nine CBCT units. Dentomaxillofac Radiol 2015;44(1):20140197https://doi.org/10.1259/dmfr.20140197. Erratum in: Dentomaxillofac Radiol. 2015;44(7):20159003. PMID: 25224586; PMCID: PMC4277438.